Joule heating synthesis of well lattice-matched $Co_2Mo_3O_8/MoO_2$ heterointerfaces with greatly improved hydrogen evolution reaction in alkaline seawater electrolysis with 12.4 % STH efficiency

Jianpeng Sun [a], Shiyu Qin [a], Zisheng Zhang [b], Chunhu Li [a], Xiaofeng Xu [c], Zizhen Li [a], Xiangchao Meng [a],[*]

[a] *Key Laboratory of Marine Chemistry Theory and Technology (Ministry of Education), College of Chemistry & Chemical Engineering, Ocean University of China, Qingdao, Shandong 266100, China*
[b] *Department of Chemical and Biological Engineering, Faculty of Engineering, University of Ottawa, Ottawa, Ontario K1N6N5, Canada*
[c] *College of Materials Science and Engineering, Ocean University of China, Qingdao 266100, China*

ARTICLE INFO

ABSTRACT

Herein, through a rapid Joule heating method, we have successfully prepared well lattice-matched $Co_2Mo_3O_8/MoO_2$ heterointerfaces on Ni foam ($Co_2Mo_3O_8/MoO_2/NF$) in only 130 s. Notably, the rapid Joule heating can effectively avoid oxidation of catalyst caused by prolonged heating and achieve rich uncoordinated Mo^{4+} sites, which contributed to the enhanced electrocatalytic performance in hydrogen evolution reaction (HER). As-prepared $Co_2Mo_3O_8/MoO_2$ delivered remarkable HER activity (23 mV at 10 mA cm^{-2}), which was comparable to Pt-based electrocatalyst. As-prepared sample also revealed excellent stability at 200-h test in electrocatalytic splitting of alkaline seawater. Of particular note, the solar-driven H_2O-H_2 electrolyzer also showed a promising solar-to-hydrogen (STH) efficiency of 12.4 %. The cell voltage for the home-made anion exchange membrane (AEM) seawater electrolyzer was only 2.13 V at 200 mA·cm^{-2} at 50 °C, and only 4.7 kW-h required to produce 1 m^3 of H_2. DFT calculations revealed that the electron redistribution spontaneously takes place at Co–O–Mo bonds at $Co_2Mo_3O_8/MoO_2$ heterointerfaces, which could regulate the electronic structure and *d*-band center of Mo sites, and then achieve high-efficiency adsorption of H_2O on Mo sites and near-zero hydrogen-adsorption free energy on O sites. This study provided a new strategy to regulate the chemical states via Joule heating for highly efficient seawater splitting to evolve H_2.

1. Introduction

Electrocatalytic seawater splitting, as an effective method for hydrogen (H_2) production, has been considered as a promising alternative to solve the freshwater shortage crisis and meet future global energy demands [1–3]. However, when electrocatalyst is applied in seawater splitting, Cl_2 evolution reaction (CER, $2Cl^- - 2e^- \rightarrow Cl_2$) is very easy to occur at low pH or Cl^- reacts with OH^- to form hypochlorite ($Cl^- - 2e^- + 2OH^- \rightarrow ClO^- + H_2O$) at high pH on the anode, which would compete with anodic oxygen evolution reaction (OER) [4]. The medium/long-term corrosion by chloride and the existence of ions in seawater may corrode the electrocatalyst and further reduce its activity [5]. Studies have shown that in alkaline electrolytes (pH > 7.5), the initial potential of OER is lower than that of CER, and there is a window

of OER potential (overpotential ≤480 mV). It suggests that it is easy to suppress the CER via adjust the pH of the electrolytes [6]. As for the hydrogen evolution reaction (HER) occurred on cathode, highly reactive and robust electrocatalysts are urgently required to develop for highly effective splitting of seawater for H_2 production.

Molybdenum dioxide (MoO_2) have increasingly attracted attentions for their good electrical conductivity, high anti-corrosive quality as HER electrocatalysts [7–10]. However, due to insufficient exposure and poor reaction kinetic of active sites, electrocatalytic activity of MoO_2 requires to further improve for wide application. Generally, the electrocatalytic activity of MoO_2 is determined by both adsorptions of water and desorption of hydrogen from either surface Mo sites or O sites. Interface engineering, as an effective approach, can directly tune the Mo-O bonds at the interface and then tailor the binding energy, consequently
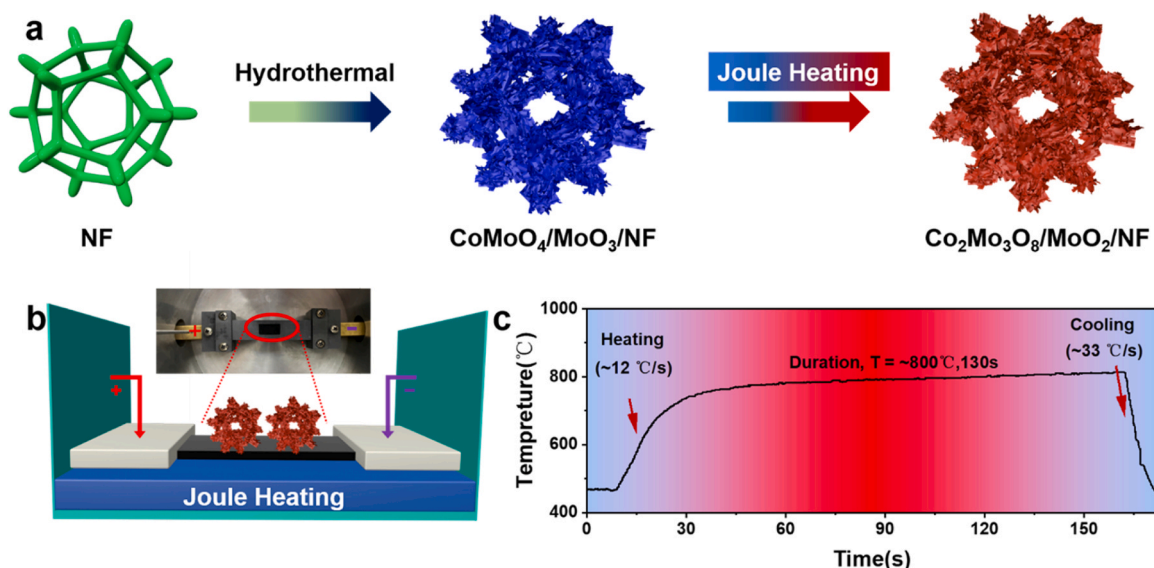
Fig. 1. (a) Schematic illustration of the synthesis of $Co_2Mo_3O_8/MoO_2/NF$. (b) Schematic diagram of Joule heating device. (c) Real time reaction temperature of Joule heating process.

accelerating the H_2 production [11–13]. For example, Yang et al. reported on an interface-rich $FeNiP/MoO_x/NiMoO_4$ heterostructures, which achieved excellent water splitting performance (1.47 V@10 mA cm^{-2}) in simulated seawater (i.e. 3.5 % NaCl aqueous solution). And the regulated electronic structure of Mo-O bonds at the interface facilitated the adsorption of H_2O and desorption of H [14]. Besides, the regulation of element valence state, especially for Mo sites with unsaturated coordination environment, is also believed to enhance the adsorption of H_2O to regulate their catalytic properties [15,16]. Unfortunately, there are few reports on regulating low element valence state of Mo sites in MoO_2-based electrocatalyst. This is mainly because the traditional synthesis methods of MoO_2, such as chemical vapor deposition (CVD), tend to require prolonged heating, which results in the over oxidation of Mo sites [17,18]. Furthermore, long time heating may further lead to aggregation and deactivation of active sites on interface [17,19,20]. Such behavior will inhibit the exposure of low-priced Mo sites and reduce the performance of electrocatalysts. Therefore, the further development of an effective method to fabricate of MoO_2-based electrocatalyst is of great significance for the design of cost-efficient electrocatalysts.

Recently, Joule heating effect has been applied to rapidly synthesize highly-efficiently functional materials, which can reach an ultrahigh temperature (>2000 K) in a short time ($\approx$12 ms) and avoid the accumulation of active sites in the process of long-time heating [21–23]. Meanwhile, rapid cooling also easily leads to structural distortions and lattice strain, thus providing rich uncoordinated catalytic sites. For example, Hu et al. designed a FeS_2 nanoparticles in reduced graphene oxide (RGO) via directly Joule heating [24]. Benefiting from rapid cooling process, iron and sulfur atoms nucleated around the base surface defects of RGO nanosheets and finally achieved a good HER activity (139 mV@10 mA cm^{-2}). Therefore, rapid Joule heating is expected to compensate for the problem of oxidation, aggregation and deactivation of active sites on interface of catalysts during conventional heating, and might achieve rich uncoordinated Mo sites. However, no relevant research about Joule heating effect has been conducted to design and synthesize MoO_2-based electrocatalyst. Moreover, the use of Ni foam (NF) and Cu foam (CF) can effectively avoid the problem of powder catalyst falling off easily. And the three-dimensional (3D) morphology, hole structure and conductive substrate can improve the specific surface area, accelerate electron transfer and increase the active site, which is conducive to H_2 release [25].

Based on the above consideration, we first constructed a novel well lattice-matched $Co_2Mo_3O_8/MoO_2$ on nickel foam ($Co_2Mo_3O_8/MoO_2/NF$) electrocatalyst enriched with uncoordinated Mo^{4+} sites via rapid Joule heating. During the Joule heating process, $Co_2Mo_3O_8/MoO_2/NF$ exposed abundant $Co_2Mo_3O_8$ and MoO_2 compatible interfaces and lattice dislocations, which can result in electronic rearrangement on the heterogeneous interface, enhance Mo-O bonds at the interface and then optimize the activity of active sites. As a result, $Co_2Mo_3O_8/MoO_2/NF$ showed excellent HER activity and stability in seawater splitting and anion exchange membrane (AEM) seawater electrolyzer. Finally, the mechanistic insights of as-prepared sample were explored via experimental and theoretical research.

2. Preparation of nanomaterials

2.1. Preparation of $CoMoO_4/MoO_3/NF$

First, hydrochloric acid (2 M) were used to clean and remove impurities on the commercial nickel foam (NF). And then, $Co(NO_3)_2\cdot6\ H_2O$ (350 mg) and $(NH_4)_6Mo_7O_{24}4H_2O$ (370 mg) were separately dispersed in 30 mL of deionized (DI) water. Then, the mixture was transferred into an autoclave, and a piece of NF (2 cm × 2 cm) was vertically immersed into the solution, which was kept at 150 °C for 6 h. $CoMoO_4/MoO_3/NF$ was dried at 70 °C under vacuum, and then collected. And MoO_3/NF was designed using a method similar to the preparation method of $CoMoO_4/MoO_3/NF$ except no $Co(NO_3)_2\cdot6\ H_2O$ was added.

2.2. Preparation of $Co_2Mo_3O_8/MoO_2/NF$

Rapid Joule heating and hydrogen reduction were used to synthesize $Co_2Mo_3O_8/MoO_2/NF$. A piece of $CoMoO_4/MoO_3/NF$ (1 cm × 0.5 cm) was placed on a graphite heating plate. $CoMoO_4/MoO_3/NF$ was heated at 800 °C for 130 s under Ar-H_2 flow. And then, $Co_2Mo_3O_8/MoO_2/NF$ were collected. As a contrast, A piece of $CoMoO_4/MoO_3/NF$ (1 cm × 0.5 cm) was placed on tube furnace. $CoMoO_4/MoO_3/NF$ was heated for 2 h at 800 °C under Ar-H_2 flow. And then, $Co_3Mo/CoO/NF$ were collected. The mass loading of the catalyst was about 4 mg cm^{-2}. MoO_2/NF were prepared using a method similar to the preparation method of $Co_2Mo_3O_8/MoO_2/NF$ apart from MoO_3/NF being used to replace $CoMoO_4/MoO_3/NF$.
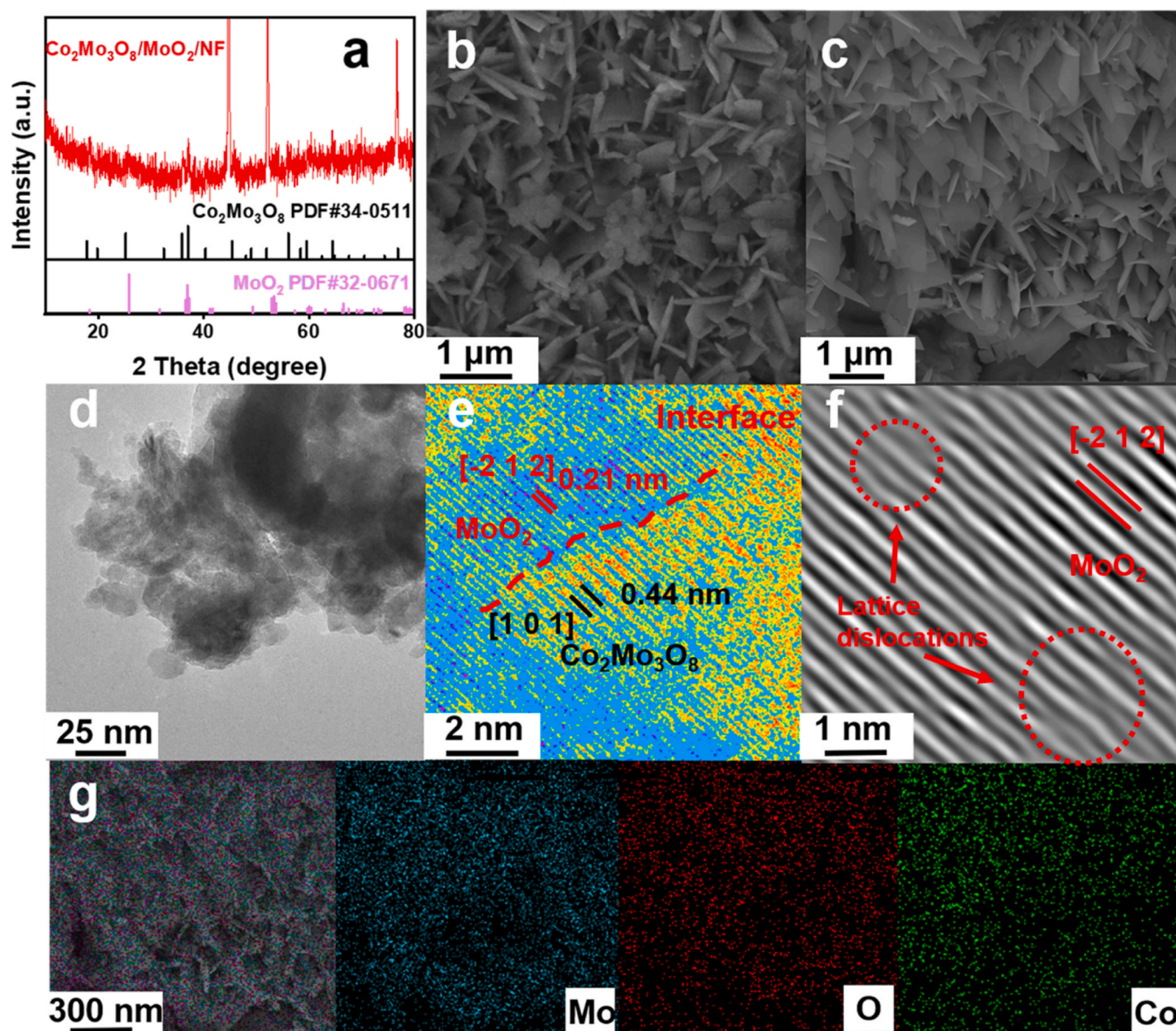
Fig. 2. (a) XRD pattern of Co$_2$Mo$_3$O$_8$/MoO$_2$/NF. (b) SEM image of CoMoO$_4$/MoO$_3$/NF. (c) SEM image, (d) TEM image, (e, f) HRTEM image and (g) EDS mapping images of Co$_2$Mo$_3$O$_8$/MoO$_2$/NF.

3. Results and discussion

3.1. Catalyst characterization and discussion

The fabrication of well lattice-matched Co$_2$Mo$_3$O$_8$/MoO$_2$ hetero-interfaces were constructed using rapid Joule heating as depicted in Fig. 1a. Firstly, CoMoO$_4$/MoO$_3$ grown on Ni foam was selected as the precursor for the synthesis of Co$_2$Mo$_3$O$_8$/MoO$_2$/NF, because their MoO$_6$ octahedral units were similar and were stacked with shared edges and/ or shared angles (Fig. S1) [10]. And then, the crystal phase of the precursor was in-situ transformed, forming a well lattice-matched Co$_2$Mo$_3$O$_8$/MoO$_2$/NF electrocatalyst through rapid Joule heating and hydrogen reduction in Ar/H$_2$ atmosphere at 800 °C for 130 s in Fig. 1b. The real time reaction temperature of Joule heating process was showed in Fig. 1c, it could be seen that the synthesis of Co$_2$Mo$_3$O$_8$/MoO$_2$/NF electrocatalyst underwent high heating (12 °C s^{-1}) and cooling processes (33 °C s^{-1}), which would lead to efficient recombination of the electronic structure of the catalyst. Meantime, affected by hydrogen reduction in an Ar/H$_2$ atmosphere, a high Mo^{6+} valence state in

CoMoO$_4$/MoO$_3$/NF was also easily transformed into low Mo^{4+} valence state in Co$_2$Mo$_3$O$_8$/MoO$_2$/NF under hydrogen reduction [17]. And low Mo valence state with unsaturated coordination environment meant a rich concentration of electrons on the surface of Mo, which was beneficial to improve the electrocatalytic activity in Co$_2$Mo$_3$O$_8$/MoO$_2$/NF [9, 16]. Meanwhile, pure MoO$_2$ supported on Ni foam were synthesized by reducing the MoO$_3$ by the same method. For comparison, CoMoO$_4$/MoO$_3$/NF were also synthesized via the CVD heating process.

As shown in XRD image (Fig. S2), it could be seen that CoMoO$_4$/MoO$_3$/NF precursor was successful synthesized on Ni foam. And XRD patterns of Co$_2$Mo$_3$O$_8$/MoO$_2$/NF were consist of both Co$_2$Mo$_3$O$_8$ (JCPDS# 34–0511) and MoO$_2$ (JCPDS# 32–0671), suggesting the successful synthesis of Co$_2$Mo$_3$O$_8$/MoO$_2$/NF in Fig. 2a. Subsequently, the detailed structural features of CoMoO$_4$/MoO$_3$/NF were verified by using SEM tests in Fig. 2b. CoMoO$_4$/MoO$_3$ nanosheets densely covered the surface of Ni foam and had a unique 3D hierarchical nanostructure. In the subsequent rapid Joule heating and hydrogen reduction process, the obtained Co$_2$Mo$_3$O$_8$/MoO$_2$/NF still well maintained the hierarchical nanostructure and possessed abundant interconnected nanosheets with
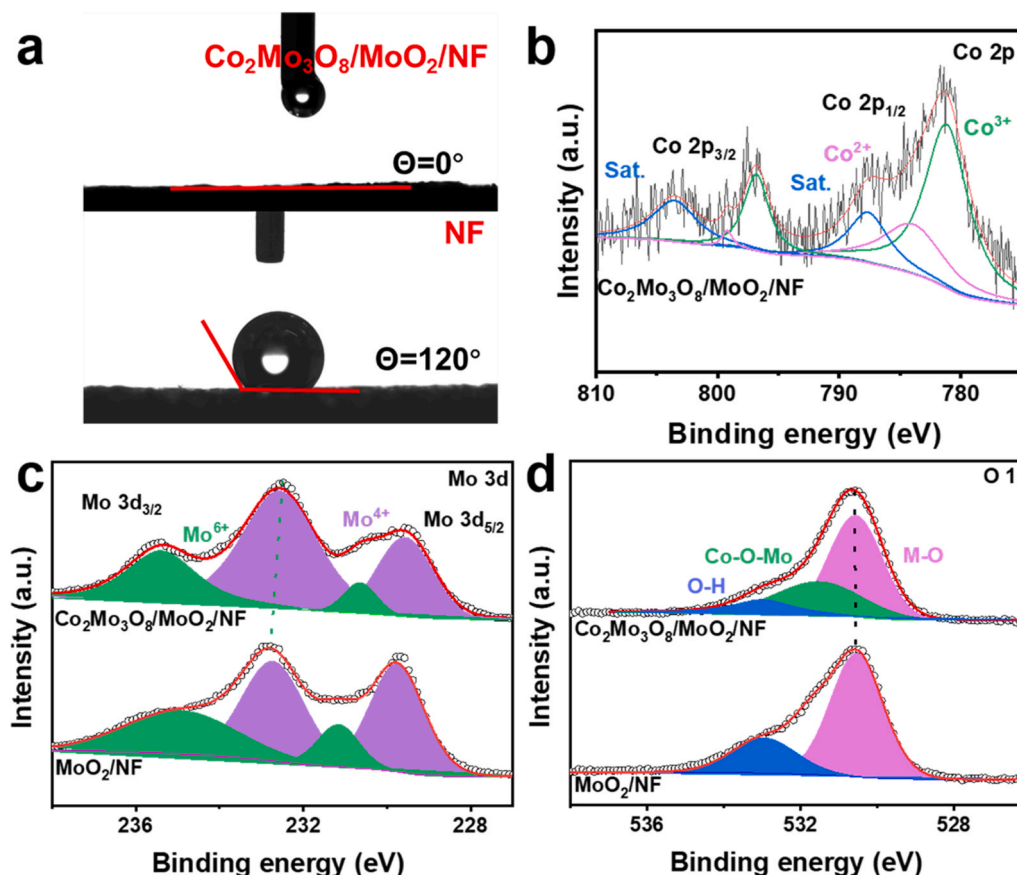
Fig. 3. (a) The droplet contact angle images of the bare NF and Co₂Mo₃O₈/MoO₂/NF. HR-XPS spectra of (b) Co 2p, (c) Mo 3d and (d) O 1 s.

smooth surfaces in Fig. 2c. This unique nanosheet structure could provide enough space to promote the diffusion and penetration of electrolyte and facilitate the dissipation of the generated gas bubbles from surface, which was crucial for improving electrochemical HER activity, especially at high current densities [26,27]. As expected, due to its similar MoO_6 octahedral units, its crystals were very easily transformed under hydrogen reduction conditions. TEM image (Fig. 2d) also showed the nanosheet structure of $Co_2Mo_3O_8/MoO_2/NF$. From HRTEM images (Figs. S3 and 2e) of $Co_2Mo_3O_8/MoO_2/NF$, the measured interspaces of 0.21 nm and 0.44 nm were well correlated with the $(-2\ 1\ 2)$ face of MoO_2 phase and the $(1\ 0\ 1)$ face of the $Co_2Mo_3O_8$ phase, respectively. Notably, it had familiar lattice trends and excellent lattice matching in $Co_2Mo_3O_8/MoO_2/NF$. Meanwhile, Fig. 2f showed lattice dislocations in the images of the $(-2\ 1\ 2)$ face of MoO_2 phase, which was attributed to the rapid heating and cooling processes under Joule heating process [28]. Such unique structure in $Co_2Mo_3O_8/MoO_2/NF$ could optimize the electronic structure and provide rich uncoordinated catalytic sites, which was a vital feature for promoting electrocatalysis. Meanwhile, the interface with good lattice matching was also expected to enhance the stability in seawater splitting. Furthermore, the energy-dispersive X-ray spetroscopy showed the uniform distribution of Co, O and Mo species in Fig. 2g and S4. And ICP-OES result showed the Co and Mo wt% were 8.76 % and 24.2 % in $Co_2Mo_3O_8/MoO_2/NF$, respectively. Furthermore, Fig. S5 exhibited that after forming lattice-matched $Co_2Mo_3O_8/MoO_2$ heterointerfaces on Ni foam, specific surface area of $Co_2Mo_3O_8/MoO_2/NF$ was 14.56 $m^2\ g^{-1}$, which was better than MoO_2/NF (11.82 $m^2\ g^{-1}$), suggested that nanosheets could enlarge the surface area [29].

To further contrast the difference between Joule heat and CVD process, the corresponding XRD and HRTEM of CVD heating process was also tested, it could be seen that catalysts had a typical peak of Co_3Mo and CoO in Fig. S6, which was attributed to the long-term hydrogen

reduction leading to further reduction of $Co_2Mo_3O_8/MoO_2$, and then transformed into a Co_3Mo-CoO/NF catalyst [12,30]. HRTEM showed that the measured interspaces of 0.16 nm and 0.39 nm were well correlated with the $(1\ 0\ 1)$ face of Co_3Mo phase and the $(3\ 1\ 1)$ face of the CoO phase, respectively. Notably, there were no obvious interfaces in Co_3Mo-CoO/NF compared with $Co_2Mo_3O_8/MoO_2/NF$. In all, the compatibility interface was attributed to the fact that part of the lattice was not completely transformed during rapid cooling process of Joule heating.

Moreover, to further prove the advatange of nanosheet structure of $Co_2Mo_3O_8/MoO_2/NF$, the hydrophilicity of $Co_2Mo_3O_8/MoO_2/NF$ and bare NF was tested in Fig. 3a. Water contact angle on NF was measured as 120°, which was signifcantly reduced to 0 ° on $Co_2Mo_3O_8/MoO_2/NF$. This result suggested that a superhydrophilic surface was estabilished on NF after modification with $Co_2Mo_3O_8/MoO_2$. It is apparent that water was easy to penetrate into $Co_2Mo_3O_8/MoO_2/NF$, which favored the high electrocatalytic activity in water splitting [31–33].

The change of the surface chemical components and electronic interactions was also important for improving the activity of the catalyst. And the surface valence state of element in $Co_2Mo_3O_8/MoO_2/NF$ and MoO_2/NF were conducted by XPS. Fig. S7 exhibited that all peaks can confirm the existence of Mo, O and Co and Ni. Ni elements came from nickel foam. High-resolution XPS (HR-XPS) orbital scans for Mo, O and Co of $Co_2Mo_3O_8/MoO_2/NF$ and MoO_2/NF were compared in Fig. 3b-d. In the Co 2p spectrum, typical peaks of Co^{3+} and Co^{2+} corresponding to $Co_2Mo_3O_8/MoO_2/NF$ were exhibited in Fig. 3b [34]. There are two typical species of Mo^{6+} and Mo^{4+} in Mo 3d spectrum of $Co_2Mo_3O_8/MoO_2/NF$ and MoO_2/NF in Fig. 3c. Notably, compared with Mo 3d spectrum of MoO_2/NF, $Co_2Mo_3O_8/MoO_2/NF$ had a negative shift by ~0.30 eV of peak, indicating the strong electronic interaction between $Co_2Mo_3O_8$ and MoO_2 interface [29,35,36]. In addition, the content (69
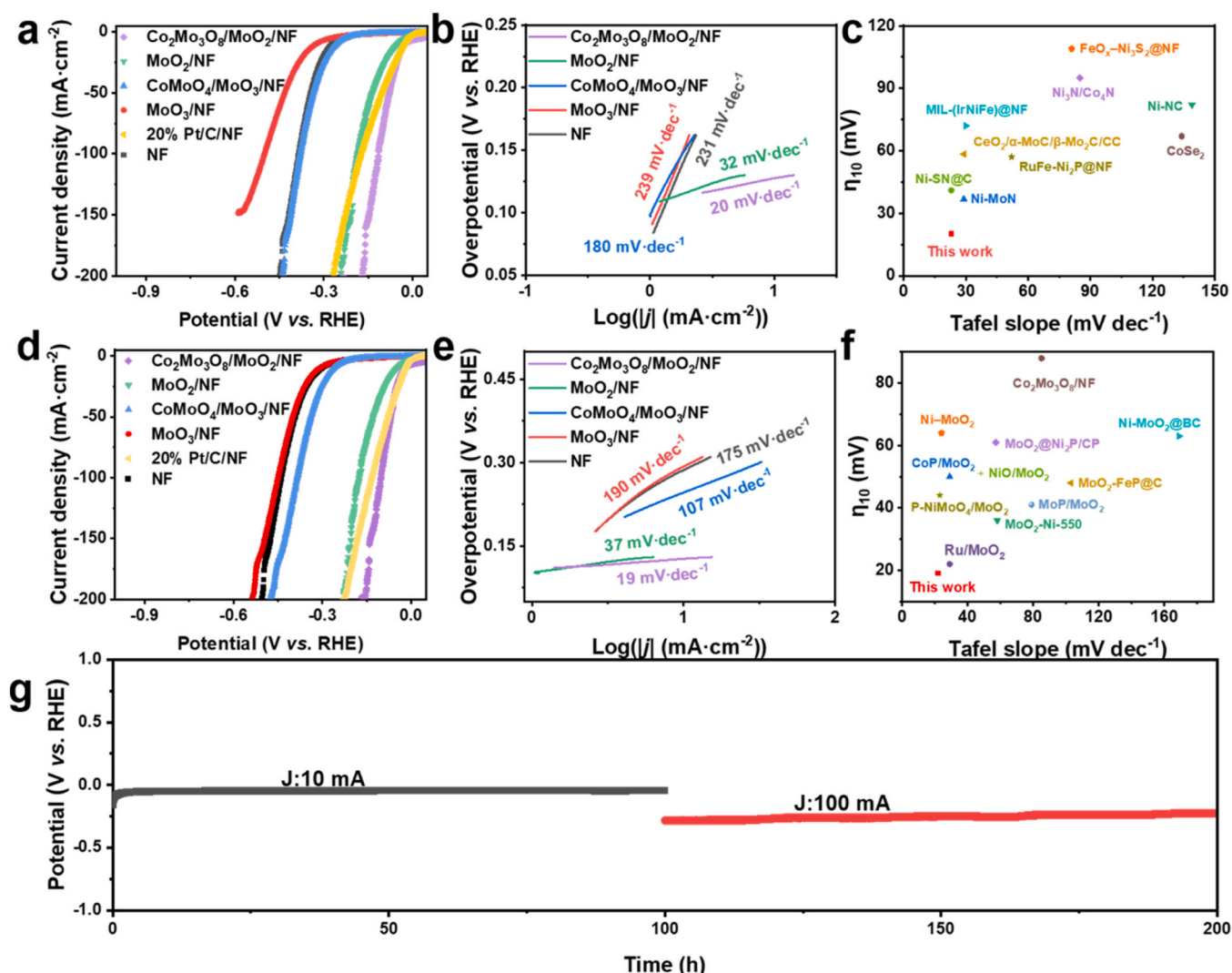
Fig. 4. (a) HER polarization curves. (b) Tafel plots. (c) η_{10} against Tafel slope profile of $Co_2Mo_3O_8/MoO_2/NF$ and the best HER electrocatalysts in recent literatures in 1.0 M KOH seawater soultion. (d) HER polarization curves. (e) Tafel plots. (f) η_{10} against Tafel slope profile of $Co_2Mo_3O_8/MoO_2/NF$ and the best HER electrocatalysts in recent literatures in 1.0 M KOH solution. (g) Long-term stability measurements of $Co_2Mo_3O_8/MoO_2/NF$.

%) of low Mo valence state (surface Mo^{4+}) of $Co_2Mo_3O_8/MoO_2/NF$ was significantly higher than Mo in MoO_2/NF (65 %) and Co_3Mo-CoO/NF (59 %) during CVD heating process in Fig. S8a [30]. Notably, rapid Joule heating lowered the problem of oxidation, aggregation and deactivation of Mo sites and achieved rich uncoordinated Mo^{4+} sites. And uncoordinated Mo^{4+} sites in $Co_2Mo_3O_8/MoO_2/NF$ could realize electron aggregation on Mo sites, which was important to enhance the adsorption of H_2O to regulate the activity of Mo sites in $Co_2Mo_3O_8/MoO_2/NF$ [9,16]. For O 1 s in Fig. 3d, it can be fitted into three characteristic peaks for the $Co_2Mo_3O_8/MoO_2/NF$. The peak located at 530.87 eV could be indexed to M–O (M = Co and Mo) bonds in $Co_2Mo_3O_8/MoO_2/NF$ [20,37]. And the peak located at 531.80 eV could be attributed to the Co–O–Mo bonds [38]. And the other peak centered at 533.13 eV can be representative adsorbed H_2O species, respectively [17]. It can be seen that after forming the interface of $Co_2Mo_3O_8/MoO_2$, the binding energy of M–O increased by ~0.10 eV compared with MoO_2/NF, indicating that the electron density on O was reduced, which was very conducive to the desorption of the final hydrogen product. Meantime, it could be seen that the binding energy of the M–O bond in $Co_2Mo_3O_8/MoO_2/NF$ had a negative shift in Fig. S8b, which meant $Co_2Mo_3O_8/MoO_2/NF$ had more electrons gathered on M–O bond, which could optimize the H adsorption kinetic. Overall, considering the peaks of Mo 3d and O 1 s shifted comparable to that in MoO_2/NF, which suggested electron

redistribution occurred in lattice-matched $Co_2Mo_3O_8/MoO_2$ heterointerfaces, which was in favor of highly efficient electrocatalyst. Based on the above results, designing lattice-matched $Co_2Mo_3O_8/MoO_2$ heterointerfaces and rapid Joule heating process in $Co_2Mo_3O_8/MoO_2/NF$ could effectively optimize the Mo–O bonds and regulate the electronic structure of surface Mo sites and O sites, which could realize rich uncoordinated Mo^{4+} sites and lower the electron density on O atoms, and thus optimize its ability to adsorb H_2O and hydrogen proton (H*).

3.2. Electrochemical HER performance

The electrocatalytic performance of $Co_2Mo_3O_8/MoO_2/NF$, MoO_2/NF, $CoMoO_4/MoO_3/NF$, MoO_3/NF and NF toward HER were measured in 1.0 M KOH seawater and 1.0 M KOH solutions, respectively. As expected, $Co_2Mo_3O_8/MoO_2/NF$ showed favorable hydrogen evolution activity with a small overpotential of 23 mV at 10 mA·cm^{-2}, which was significantly lower than MoO_2/NF (51 mV), $CoMoO_4/MoO_3/NF$ (253 mV) and MoO_3/NF (325 mV) in Fig. 4a. Meantime, the activity of $Co_2Mo_3O_8/MoO_2/NF$ was better than Pt/C (26 mV). Particularly, $Co_2Mo_3O_8/MoO_2/NF$ required only 118 at 100 mA cm^{-2}, which was better than MoO_2/NF (187 mV), $CoMoO_4/MoO_3/NF$ (379 mV), MoO_3/NF (503 mV) and Pt/C (166 mV). To further studied the effect of heterointerface formation on MoO_2, we tested and compared the

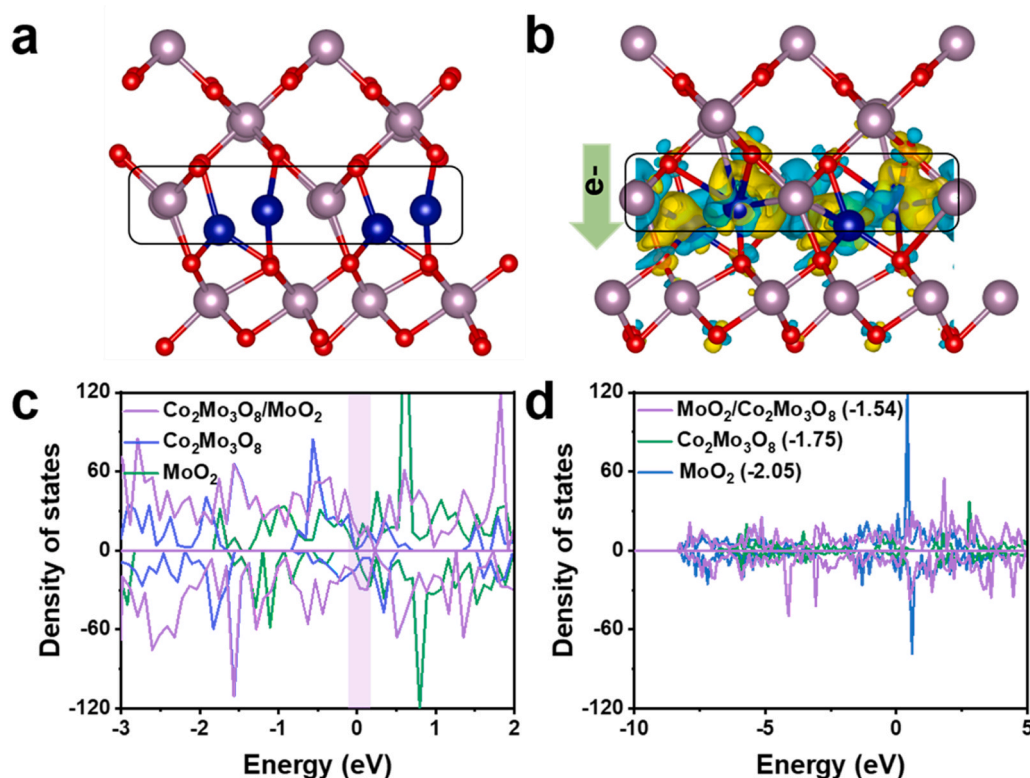**Fig. 5.** (a, b) Atomic models with charge density difference plot of $Co_2Mo_3O_8/MoO_2/NF$. (c) TDOS and (d) *d*-band center.

$Co_2Mo_3O_8/MoO_2/NF$ catalysts with different cobalt content in Fig. S10. Notably, $Co_2Mo_3O_8/MoO_2/NF$ catalysts with different cobalt content all showed excellent activity than MoO_2/NF. Meanwhile, the formation of Co-O-Mo bonds in $Co_2Mo_3O_8/MoO_2$ could be found in O1s peak of $Co_2Mo_3O_8/MoO_2/NF$ in Fig. S11. This could be used to explained the positive effect of heterointerface formation on MoO_2. These results showed that lattice-matched $Co_2Mo_3O_8/MoO_2$ was great potential for industrial seawater splitting applications. $Co_2Mo_3O_8/MoO_2/NF$ also exhibited a good HER activity compared with Co_3Mo-CoO/NF (56 mV at 10 mA·cm^{-2}) in CVD heating process in Fig. S9, which was because the joule heating process can avoid oxidation of catalyst caused by prolonged heating, achieve abundant Mo^{4+}, which was beneficial to enhance the electrocatalytic activity of MoO_2. Tafel slope measurements were applied in further investigating the reaction kinetics [39]. Fig. 4b illustrated that the Tafel value (20 mV·dec^{-1}) of $Co_2Mo_3O_8/MoO_2/NF$ was much lower than those of MoO_2/NF (32 mV·dec^{-1}), $CoMoO_4$-MoO_3/NF (180 mV·dec^{-1}), MoO_3/NF (239 mV·dec^{-1}) and NF (231 mV·dec^{-1}), meant that reaction kinetics of $Co_2Mo_3O_8/MoO_2/NF$ was drastically changed and the reaction kinetics belonged to the Volmer-Tafel reaction pathway [40]. Remarkably, $Co_2Mo_3O_8/MoO_2/NF$ displayed superior electrocatalytic activity and low Tafel slope among recently reported electrocatalysts in Fig. 4c. Such enhanced electrocatalytic activity may be because (i) unique electronic structure of lattice matching and lattice dislocations in $Co_2Mo_3O_8/MoO_2/NF$ could change the electronic structure and speed up electron transfer, thus enhance the conductivity; (ii) Rapid Joule heating process could achieve abundant rich uncoordinated Mo^{4+} sites, which could realize electron aggregation on Mo sites and then enhance the adsorption of H_2O to regulate the activity of Mo sites in $Co_2Mo_3O_8/MoO_2/NF$.

The double-layer capacitance (C_{dl}) and Nyquist diagram were used to further estimate the catalytic performance of the prepared sample in Figs. S12-S14 [35]. The lattice-matched $Co_2Mo_3O_8/MoO_2/NF$ showed a high C_{dl} value (239 mF·cm^{-2}), which was better than MoO_2/NF (245 mF·cm^{-2}), $CoMoO_4/MoO_3/NF$ (3.3 mF·cm^{-2}) and MoO_3/NF (2.6 mF·cm^{-2}) in Fig. S13. This result suggested that the lattice-matched

$Co_2Mo_3O_8/MoO_2/NF$ possessed a large electrochemically active surface areas (ECSA), which could provide more reactive sites in seawater hydrogen evolution. Moreover, $Co_2Mo_3O_8/MoO_2/NF$ also showed smallest Nyquist plots among the afore mentioned electrocatalysts (Fig. S14), which further indicated that $Co_2Mo_3O_8/MoO_2/NF$ had faster charge transfer and good reaction kinetic. Moreover, the HER activity was studied in 1.0 M KOH solution. Notably, $Co_2Mo_3O_8/MoO_2/NF$ maintained excellent activity, which only needed 22 mV at 10 mA·cm^{-2} and low Tafel slope (19 mV dec^{-1}) in Fig. 4d and e. Meanwhile, the activity at 10 mA·cm^{-2} of $Co_2Mo_3O_8/MoO_2/NF$ was closed to that of Pt/C (20 mV). In all, $Co_2Mo_3O_8/MoO_2/NF$ revealed excellent electrocatalytic activity at 10 mA cm^{-2} among recently reported Mo-based electrocatalysts in Fig. 4f. Furthermore, long-term stability of $Co_2Mo_3O_8/MoO_2/NF$ in 1.0 M KOH seawater was tested by amperometric stability (Fig. 4g). It could be seen that there was almost no decay for 200 h. Meanwhile, XPS and SEM tests after long-term stability measurements were showed in Fig. S15. It could be seen that the peaks of Co, Mo and O had no obvious change. But the peak of Mo had slightly decreased, indicating more electrons gathered on Mo sites to regulate the H adsorption kinetics. And SEM also confirmed that nanosheets morphology was maintained without change. And a photograph of the electrode was taken in Fig. S15d, there was almost no precipitation observed. Furthermore, ICP-OES of seawater after 200 h-stability was tested and there was very little dissolution of Co (0.007 mg/L), which meant the catalyst exhibited that lattice-matched $Co_2Mo_3O_8/MoO_2/NF$ possessed the high structural and good commercialization prospects for seawater splitting.

Additionally, OER performance of $Co_2Mo_3O_8/MoO_2/NF$, MoO_2/NF, $CoMoO_4/MoO_3/NF$, MoO_3/NF and NF were also evaluated in 1.0 M KOH seawater and 1.0 M KOH solutions. Fig. S16 showed $Co_2Mo_3O_8/MoO_2/NF$ had a favorable OER activity with a small overpotential of 320 mV and 270 mV at 40 mA cm^{-2} in 1.0 M KOH seawater and 1.0 M KOH solutions, respectively. And $Co_2Mo_3O_8/MoO_2/NF$ exhibited excellent OER performance, which meant that well lattice-matched $Co_2Mo_3O_8/MoO_2/NF$ had a good commercialization prospects of
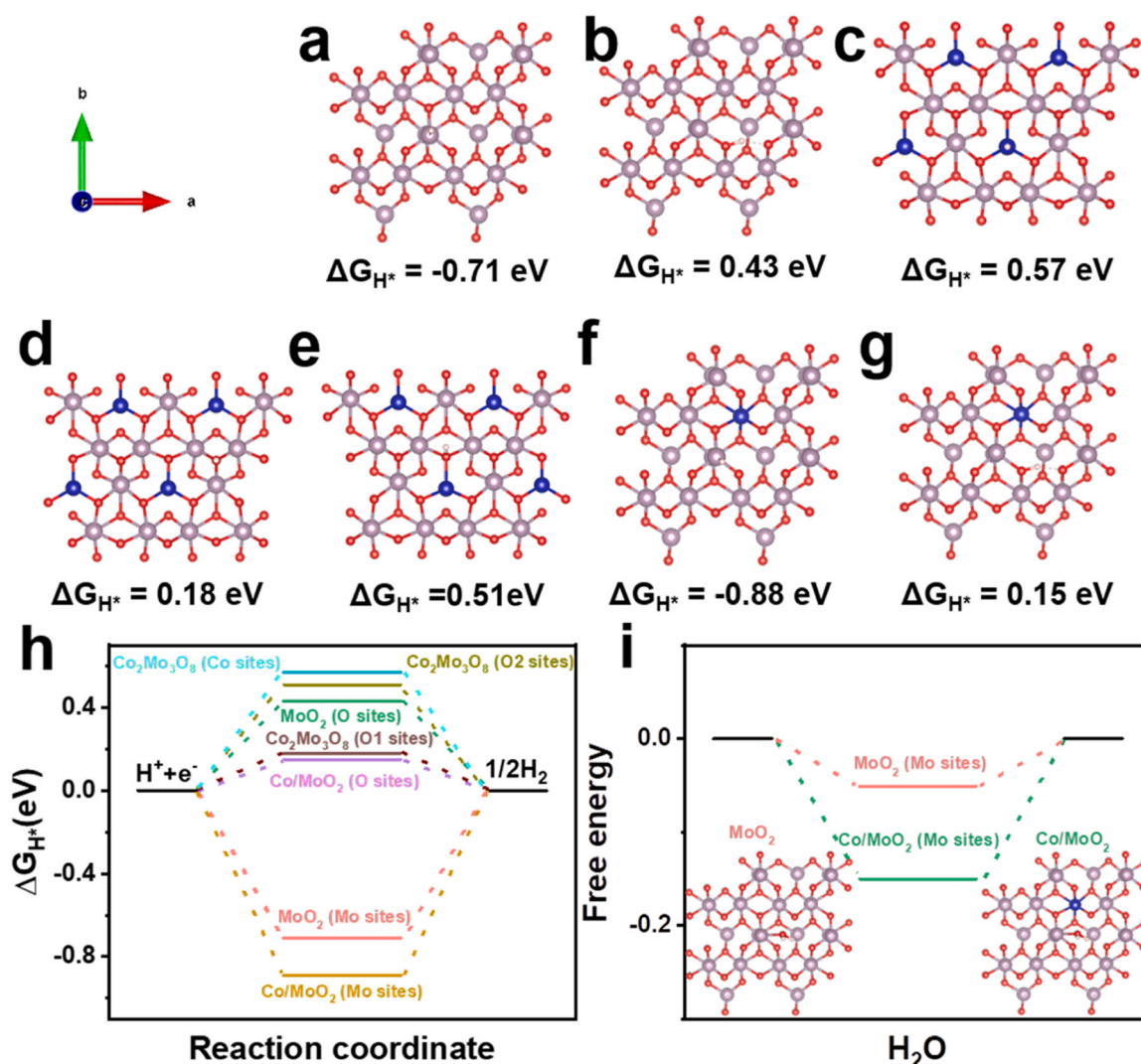
Fig. 6. The top-view schematic models of (a) MoO_2-Mo sites, (b) MoO_2-O sites, (c) $Co_2Mo_3O_8$-Mo sites, (d) $Co_2Mo_3O_8$-O1 sites, (e) $Co_2Mo_3O_8$-O2 sites, (f) Co/MoO_2-Mo sites and (g) Co/MoO_2-O sites. (h) ΔG_{H*}. (i) H_2O adsorption energy.

electrocatalysts in overall seawater splitting.

3.3. DFT calculations

DFT calculations were applied to access the electronic structure and corresponding Gibbs free energy (ΔG) on the lattice-matched $Co_2Mo_3O_8$/MoO_2/NF heterointerfaces. For comparison, pure $Co_2Mo_3O_8$ and MoO_2 were also studied via theoretical calculations. To study the electron interaction at the $Co_2Mo_3O_8$/MoO_2 heterostructures, the localized charge distribution in $Co_2Mo_3O_8$/MoO_2 was simulated. As expected, affected by the formation of $Co_2Mo_3O_8$/MoO_2 hetero-interfaces, the charge transfer path was destroyed and abundant charge gathered at the interface in Fig. 5a and b, which resulted in a non-uniform charge distribution and electron redistribution, and then opti-mized the electronic structure and achieved the fast electrons transfer rate of MoO_2 [41,42]. Furthermore, the DOS of $Co_2Mo_3O_8$, MoO_2 and $Co_2Mo_3O_8$/MoO_2 was investigated in Fig. S17. It could be seen that MoO_2, $Co_2Mo_3O_8$ and $Co_2Mo_3O_8$/MoO_2 exhibited good conductivity due to their metallic character with zero bandgap [43,44]. After forming well lattice-matched heterostructures, the TDOS of $Co_2Mo_3O_8$/MoO_2 was higher than that of $Co_2Mo_3O_8$ and MoO_2 in Fig. 5c, suggesting that the electron rearrangement at the $Co_2Mo_3O_8$/MoO_2 heterostructures could optimize the electronic structure and achieve a good electrical conductivity.

Previous study showed that Mo sites could not only promote the capture of H_2O molecules, but also optimize the kinetics of hydrogen adsorption and desorption [45–47]. And d-band center of Mo sites was used to reflect the electronic interactions between reaction in-termediates and Mo sites. It could be seen that the d-band center of Mo in $Co_2Mo_3O_8$/MoO_2 was −1.54 eV, which was better than $Co_2Mo_3O_8$ (−1.75 eV) and MoO_2 (−2.05 eV) in Fig. 5d, indicating that well lattice-matched $Co_2Mo_3O_8$/MoO_2 heterostructures had strong electronic interaction between H_2O/H* and Mo sites. The strong Mo-H_2O/H* interaction could promote the adsorption of reaction intermediates at Mo sites, which was key to improve the HER activity of materials.

To directly study the influence of interfacial Mo-O structure on the relationship between reaction intermediates and catalysts, the corre-sponding ΔG was calculated in Fig. 6. First, the adsorption energy of H* (ΔG_{H*}) at the different active sites of $Co_2Mo_3O_8$ and MoO_2 were calcu-lated in Fig. 6a-e and S18. When ΔG_{H*} of active sites was close to 0, which meant that active sites had a good H* adsorption energy [48–50]. As displayed in Fig. 6a-e, ΔG_{H*} values on O sites in MoO_2 (0.43 eV) or $Co_2Mo_3O_8$ (0.18 eV) were better than that on Mo sites (−0.71 eV) in MoO_2 or Co sites (0.57 eV) in $Co_2Mo_3O_8$, suggesting that O sites were more reactive active for the adsorption of H* intermediates in MoO_2 and $Co_2Mo_3O_8$. Meantime, forming lattice-matched $Co_2Mo_3O_8$/MoO_2
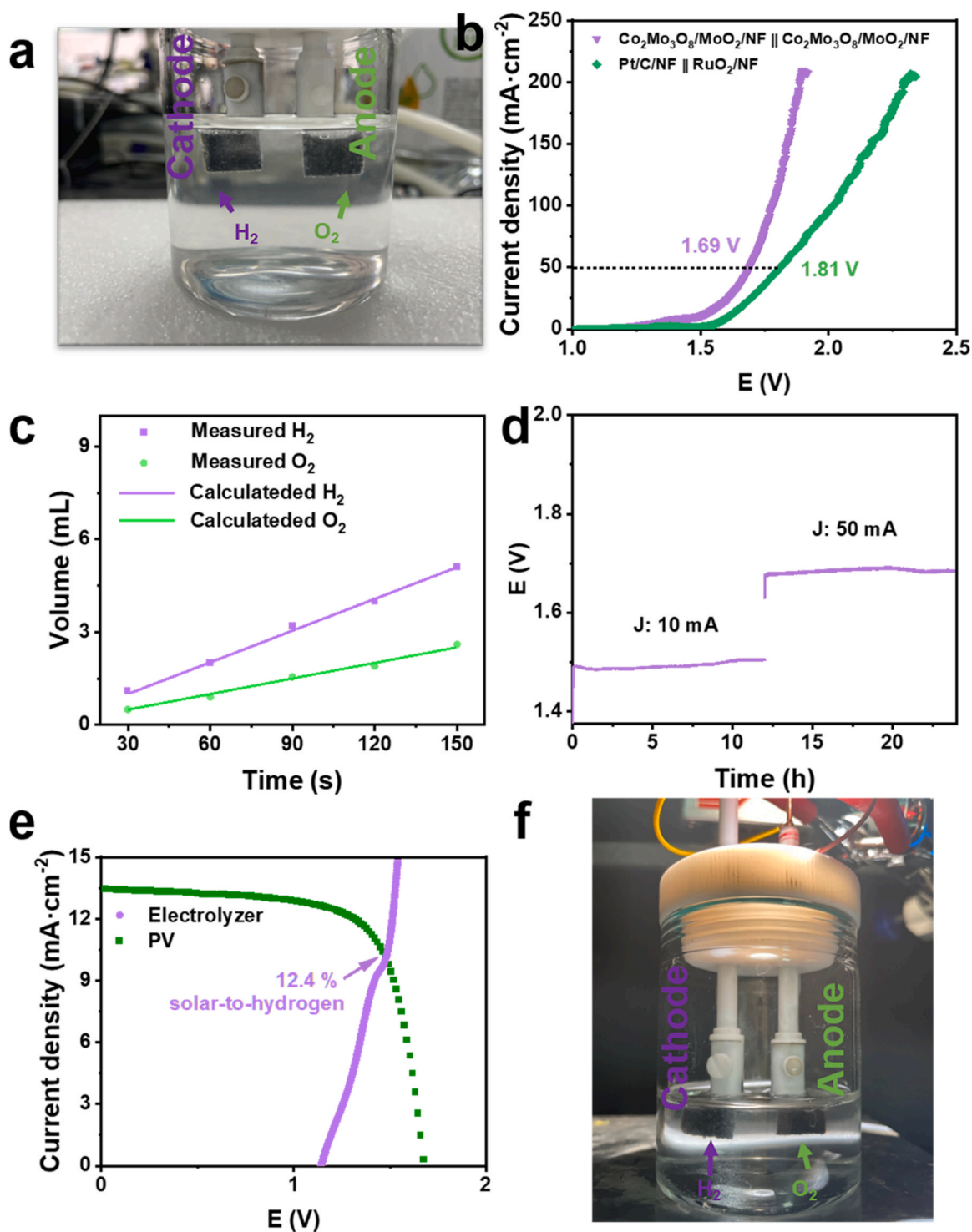
Fig. 7. (a) Photo of two-electrode cell toward overall water splitting. (b) LSV curves of the electrolyzer. (c) Device diagram for measuring Faraday efficiency. (d) Long-term stability measurements of $Co_2Mo_3O_8/MoO_2/NF$. (e) Current density–potential curves of the seawater electrolyzer and triple-junction solar cell. (f) Typical picture exhibiting the generation of H_2 gas during overall seawater splitting.

heterointerfaces, Co–O–Mo bonds was formed in $Co_2Mo_3O_8/MoO_2/NF$. And then, the $Co\text{-}MoO_2$ model were optimized to study the effect of Co–O–Mo bonds in $Co_2Mo_3O_8/MoO_2/NF$. Notably, ΔG_{H^*} values on O sites in $Co_2Mo_3O_8/MoO_2/NF$ decreased significantly, which only had 0.15 eV and suggested that Co–O–Mo bonds in heterointerfaces could effectively regulate the adsorption of H* and promote the release of H_2 [51]. In alkaline conditions, H_2O adsorption was the rate-determining step (RDS) of hydrogen evolution reaction [52,53]. And the

corresponding H_2O adsorption energy of $Co_2Mo_3O_8/MoO_2$, $Co_2Mo_3O_8$ and MoO_2 were calculated. Obviously, the value (−0.15 eV) of $Co_2Mo_3O_8/MoO_2$ are higher than that of MoO_2 (−0.05 eV) in Fig. 6i, which suggested Co-O-Mo bonds in $Co_2Mo_3O_8/MoO_2$ heterointerfaces could enhance H_2O adsorption and then optimize the HER activity in alkaline seawater splitting.
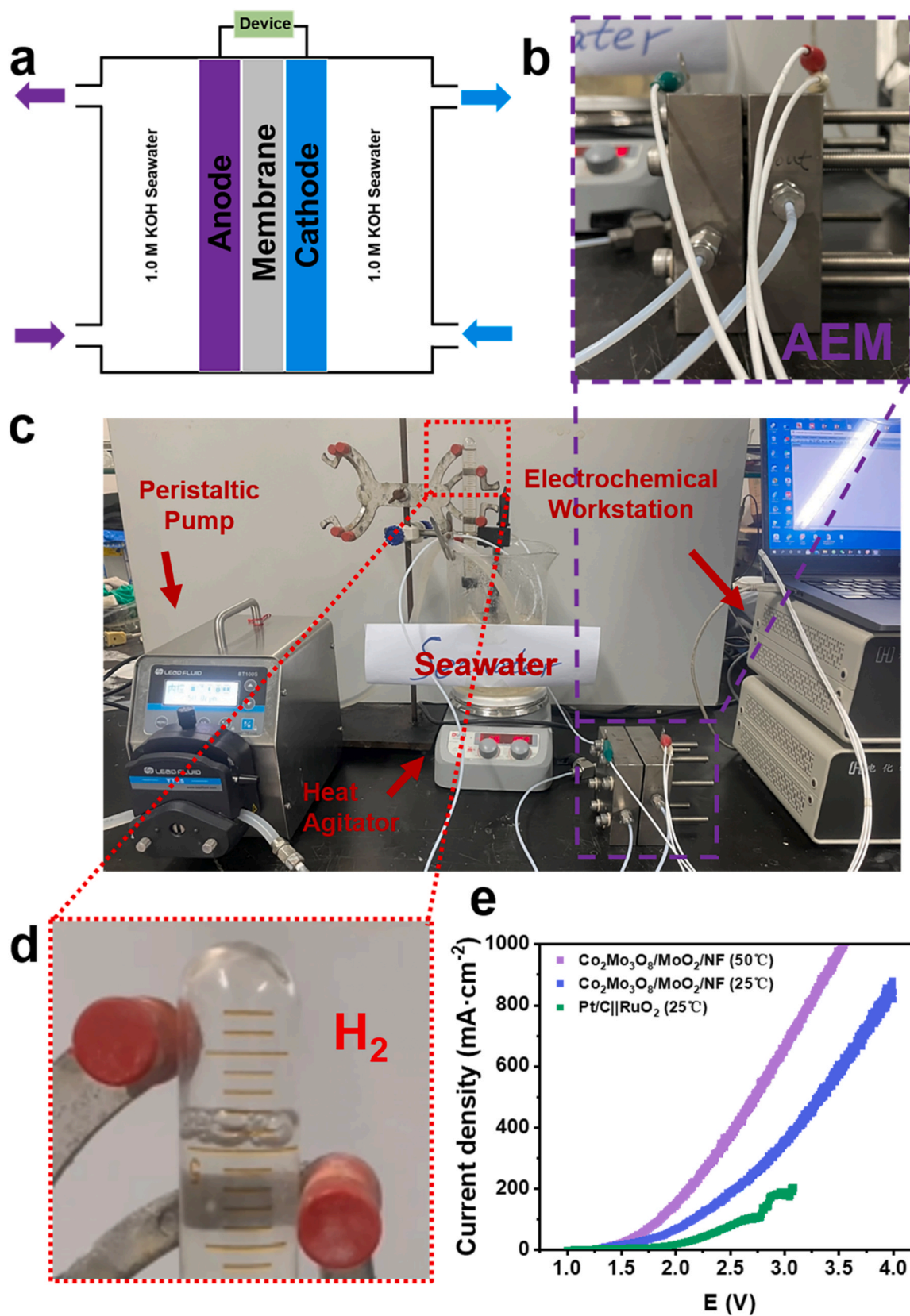
Fig. 8. (a) Schematic picture of AEM seawater electrolyzer. (b, c) Typical picture of AEM water electrolyzer. (d) Diagram of hydrogen collection device. (e) LSV curves of the electrolyzer.

3.4. Overall seawater-splitting measurement

Encouraged by the excellent activity of well lattice-matched $Co_2Mo_3O_8/MoO_2$ in alkaline seawater, an electrolytic cell was constructed by using $Co_2Mo_3O_8/MoO_2/NF$ as cathode and anode material in Fig. 7a. $Co_2Mo_3O_8/MoO_2/NF$ merely required a cell voltage of 1.69 V at 50 mA cm^{-2} in alkaline seawater, which was lower than Pt/C/NF// RuO_2/NF (1.81 at 50 mA cm^{-2}) in Fig. 7b. Additionally, Faraday efficiency (FE) were studied via comparing the ratio of actual H_2 and O_2 production in the H-type electrolytic cell (Fig. 7c). Notably, the amount of evolved H_2 and O_2 production could meet the theoretical hydrogen production, which suggested that the FE was nearly 100 % and $Co_2Mo_3O_8/MoO_2/NF$ had high selectivity in electrocatalytic seawater splitting [54,55]. Finally, $Co_2Mo_3O_8/MoO_2/NF$ still showed outstanding durability after 24 h of continuous seawater electrolysis at 10/50 mA cm^{-2} in Fig. 7d. Furthermore, the photo-driven water-splitting system was coupled with the solar cell under simulated AM1.5-G 100 mW cm^{-2} illumination. Fig. 7e showed the current density of the electrolyzer at its intersection is about 10.1 mA cm^{-2}, which represented a significant 12.4 % STH conversion efficiency in alkaline seawater splitting, which meant $Co_2Mo_3O_8/MoO_2/NF$ had a potential application in a photo-driven water-splitting system [56]. And there were many bubbles could be produced in Fig. 7f. These results of all the electrochemical tests above demonstrated that $Co_2Mo_3O_8/MoO_2/NF$ had great potential in AEM electrolyzers.

3.5. AEM electrolyzer measurement

To further study the electrocatalytic performance of $Co_2Mo_3O_8/MoO_2/NF$ in practical devices, AEM electrolyzer were constructed to study the actual hydrogen production and power consumption [57,58]. The components inside the AEM water electrolyzer were shown in Fig. 8a–d. It could be seen that AEM water electrolyzer had a significant H_2 bubble formation in Fig. 8d. The cell voltage of the AEM water electrolyzer with the $Co_2Mo_3O_8/MoO_2/NF$ catalyst was significantly lower than that of Pt/C/NF//RuO$_2$/NF material. The cell voltage (without iR compensation) for the AEM water electrolyzer with the $Co_2Mo_3O_8/MoO_2/NF$ catalyst was only 2.53 V at 200 mA cm^{-2} and 3.00 V for the unit with the Pt/C/NF//RuO$_2$/NF in Fig. 8e. Meantime, when the temperature rised to 50 °C, $Co_2Mo_3O_8/MoO_2/NF$ only needed 2.13 V at 200 mA cm^{-2}. And Corresponding power consumption were calculated, the power consumption was only 4.7 kW·h, which was much lower than Pt/C/NF//RuO$_2$/NF (6.7 kW·h). The above results confirmed that, as predicted by electrochemical measurements, the $Co_2Mo_3O_8/MoO_2/NF$ catalyst showed good activity and stability in an actual AEM seawater solution electrolyser.

4. Conclusion

In summary, the well lattice-matched $Co_2Mo_3O_8/MoO_2$ heterointerfaces on Ni foam substrate ($Co_2Mo_3O_8/MoO_2/NF$) were fabricated via a rapid Joule heating and hydrogen reduction method. And the rapid treatment at an elevated temperature promoted the formation of lattice-matched $Co_2Mo_3O_8/MoO_2/NF$, which enhanced a rich uncoordinated Mo^{4+} sites and regulate the electronic structure of O atoms. Electrochemical measurements indicated that $Co_2Mo_3O_8/MoO_2/NF$ delivered a low overpotential of 23 mV and 22 mV at 10 mA cm^2 and high stability in 1.0 M KOH seawater and 1.0 M KOH solutions, respectively. The cell voltage for the anion exchange membrane (AEM) seawater electrolyzer in our design was only 2.13 V at 200 mA·cm^{-2} at 50 °C. DFT calculations revealed the electron redistribution spontaneously takes place at the well lattice-matched $Co_2Mo_3O_8/MoO_2$ heterointerfaces, which could achieve high-efficiency adsorption of H_2O and near-zero hydrogen-adsorption free energy. This work showed that coupling catalysts with interfacial compatibility was an effective strategy to improve catalytic activity. This new type rapidly heated method by Joule heat to design well lattice-matched $Co_2Mo_3O_8/MoO_2$ heterointerfaces could open up new opportunities for the development of efficient and lasting earth rich electrocatalysts.

CRediT authorship contribution statement

Jianpeng Sun: Conceptualization, Methodology, Investigation, Writing- Original draft preparation, Writing - Review & Editing. **Shiyu Qin:** Methodology, Investigation. **Zisheng Zhang:** Methodology, Investigation, Writing - Review & Editing. **Chunhu Li:** Methodology, Investigation. **Xiaofeng Xu:** Methodology, Investigation. **Zizhen Li:** Investigation, Writing - Review & Editing. **Xiangchao Meng:** Supervision, Conceptualization, Writing - Original Draft, Writing - Review & Editing.

Declaration of Competing Interest

The authors declare that they have no known competing financial interests or personal relationships that could have appeared to influence the work reported in this paper.

Data availability

Data will be made available on request.

Appendix A. Supporting information

Supplementary data associated with this article can be found in the online version at doi:10.1016/j.apcatb.2023.123015.

References

[1] L. Yu, L. Wu, B. McElhenny, S. Song, D. Luo, F. Zhang, Y. Yu, S. Chen, Z. Ren, Ultrafast room-temperature synthesis of porous S-doped Ni/Fe (oxy)hydroxide electrodes for oxygen evolution catalysis in seawater splitting, Energy Environ. Sci. 13 (2020) 3439–3446, https://doi.org/10.1039/d0ee00921k.

[2] F. Sun, J. Qin, Z. Wang, M. Yu, X. Wu, X. Sun, J. Qiu, Energy-saving hydrogen production by chlorine-free hybrid seawater splitting coupling hydrazine degradation, Nat. Commun. 12 (2021) 4182–4192, https://doi.org/10.1038/s41467-021-24529-3.

[3] W. Tong, M. Forster, F. Dionigi, S. Dresp, R. Sadeghi Erami, P. Strasser, A.J. Cowan, P. Farràs, Electrolysis of low-grade and saline surface water, Nat. Energy 5 (2020) 367–377, https://doi.org/10.1038/s41560-020-0550-8.

[4] H. Xie, Z. Zhao, T. Liu, Y. Wu, C. Lan, W. Jiang, L. Zhu, Y. Wang, D. Yang, Z. Shao, A membrane-based seawater electrolyser for hydrogen generation, Nature 612 (2022) 673–678, https://doi.org/10.1038/s41586-022-05379-5.

[5] J.-P. Sun, Z. Zhao, J. Li, Z.-Z. Li, X.-C. Meng, Recent advances in electrocatalytic seawater splitting, Rare Met. 42 (2023) 751–768, https://doi.org/10.1007/s12598-022-02168-x.

[6] J. Sun, Y. Zhou, Z. Zhao, X. Meng, Z. Li, Modification strategies to improve electrocatalytic activity in seawater splitting: a review, J. Mater. Sci. 57 (2022) 19243–19259, https://doi.org/10.1007/s10853-022-07875-5.

[7] Y. Cao, Roadmap and direction toward high-performance MoS_2 hydrogen evolution catalysts, ACS Nano 15 (2021) 11014–11039, https://doi.org/10.1021/acsnano.1c01879.

[8] L. Najafi, S. Bellani, R. Oropesa-Nuñez, A. Ansaldo, M. Prato, A.E. Del Rio Castillo, F. Bonaccorso, Engineered $MoSe_2$-based heterostructures for efficient electrochemical hydrogen evolution reaction, Adv. Energy Mater. 8 (2018) 1703212–1703227, https://doi.org/10.1002/aenm.201703212.

[9] Y. Yang, Y. Qian, Z. Luo, H. Li, L. Chen, X. Cao, S. Wei, B. Zhou, Z. Zhang, S. Chen, W. Yan, J. Dong, L. Song, W. Zhang, R. Feng, J. Zhou, K. Du, X. Li, X.M. Zhang, X. Fan, Water induced ultrathin Mo_2C nanosheets with high-density grain boundaries for enhanced hydrogen evolution, Nat. Commun. 13 (2022) 7225–7235, https://doi.org/10.1038/s41467-022-34976-1.

[10] W. Hua, H.-H. Sun, F. Xu, J.-G. Wang, A review and perspective on molybdenum-based electrocatalysts for hydrogen evolution reaction, Rare Met. 39 (2020) 335–351, https://doi.org/10.1007/s12598-020-01384-7.

[11] F. Gong, M. Liu, S. Ye, L. Gong, G. Zeng, L. Xu, X. Zhang, Y. Zhang, L. Zhou, S. Fang, J. Liu, All-pH stable sandwich-structured MoO$_2$/MoS$_2$/C hollow nanoreactors for enhanced electrochemical hydrogen evolution, Adv. Funct. Mater. 31 (2021) 2101715–2101724, https://doi.org/10.1002/adfm.202101715.

[12] Y. Qiu, S. Liu, C. Wei, J. Fan, H. Yao, L. Dai, G. Wang, H. Li, B. Su, X. Guo, Synergistic effect between platinum single atoms and oxygen vacancy in MoO$_2$ boosting pH-Universal hydrogen evolution reaction at large current density, Chem. Eng. J. 427 (2022) 131309–131318, https://doi.org/10.1016/j.cej.2021.131309.

[13] C.-Z. Yuan, K.S. Hui, H. Yin, S. Zhu, J. Zhang, X.-L. Wu, X. Hong, W. Zhou, X. Fan, F. Bin, F. Chen, K.N. Hui, Regulating intrinsic electronic structures of transition-metal-based catalysts and the potential applications for electrocatalytic water splitting, ACS Mater. Lett. 3 (2021) 752–780, https://doi.org/10.1021/acsmaterialslett.0c00549.

[14] Z. Xiao, M. Yang, J. Wang, Z. Xu, S. Zhang, A. Tang, R. Gao, H. Yang, FeNiP/MoO$_x$ integrated electrode grown on monocrystalline NiMoO$_4$ nanorods with multi-interface for accelerating alkaline hydrogen evolution reaction, Appl. Catal. B: Environ. 303 (2022) 120913–120920, https://doi.org/10.1016/j.apcatb.2021.120913.

[15] J. Liu, L. Dong, D. Chen, Y. Han, Y. Liang, M. Yang, J. Han, C. Yang, W. He, Metal oxides with distinctive valence states in an electron-rich matrix enable stable high-capacity anodes for Li ion batteries, Small Methods 4 (2019) 1900753–1900760, https://doi.org/10.1002/smtd.201900753.

[16] G.H. Han, H. Kim, J. Kim, J. Kim, S.Y. Kim, S.H. Ahn, Micro-nanoporous MoO$_2$@ CoMo heterostructure catalyst for hydrogen evolution reaction, Appl. Catal. B: Environ. 270 (2020) 118895–118904, https://doi.org/10.1016/j.apcatb.2020.118895.

[17] C. Li, H. Jang, M.G. Kim, L. Hou, X. Liu, J. Cho, Ru-incorporated oxygen-vacancy-enriched MoO$_2$ electrocatalysts for hydrogen evolution reaction, Appl. Catal. B: Environ. 307 (2022) 121204–121211, https://doi.org/10.1016/j.apcatb.2022.121204.

[18] X. Wu, J. Li, Y. Li, Z. Wen, NiFeP-MoO$_2$ hybrid nanorods on nickel foam as high-activity and high-stability electrode for overall water splitting, Chem. Eng. J. 409 (2021), https://doi.org/10.1016/j.cej.2020.128161.

[19] W.J. Jiang, T. Tang, Y. Zhang, J.S. Hu, Synergistic modulation of non-precious-metal electrocatalysts for advanced water splitting, Acc. Chem. Res. 53 (2020) 1111–1123, https://doi.org/10.1021/acs.accounts.0c00127.

[20] H.D. Jiao-Jiao Zhou, Zile Hua, Le Xu, Weiwei Wang, Linping Wang, Lei Han, Luyang Chen, Unveiling high intrinsic activity of Co$_3$Mo alloy and metallic Ni embedded in CoNiMo-O nanosheets arrays for hydrogen evolution reaction, 138206-138015, Chem. Eng. J. 450 (2022), https://doi.org/10.1016/j.cej.2022.138206.

[21] S. Dou, J. Xu, X. Cui, W. Liu, Z. Zhang, Y. Deng, W. Hu, Y. Chen, High-temperature shock enabled nanomanufacturing for energy-related applications, Adv. Energy Mater. 10 (2020) 2001331–2001345, https://doi.org/10.1002/aenm.202001331.

[22] K. Zeng, J. Zhang, W. Gao, L. Wu, H. Liu, J. Gao, Z. Li, J. Zhou, T. Li, Z. Liang, B. Xu, Y. Yao, Surface-decorated high-entropy alloy catalysts with significantly boosted activity and stability, Adv. Funct. Mater. 32 (2022) 2204643–2204652, https://doi.org/10.1002/adfm.202204643.

[23] S. Chen, L. Nie, X. Hu, Y. Zhang, Y. Zhang, Y. Yu, W. Liu, Ultrafast sintering for ceramic-based all-solid-state lithium-metal batteries, Adv. Mater. 34 (2022) 2200430–2200439, https://doi.org/10.1002/adma.202200430.

[24] Y. Chen, S. Xu, Y. Li, R.J. Jacob, Y. Kuang, B. Liu, Y. Wang, G. Pastel, L. G. Salamanca-Riba, M.R. Zachariah, L. Hu, FeS$_2$ nanoparticles embedded in reduced graphene oxide toward robust, high-performance electrocatalysts, Adv. Energy Mater. 7 (2017) 1700482–1700488, https://doi.org/10.1002/aenm.201700482.

[25] Y. Liu, X. Zhang, W. Zhang, X. Ge, Y. Wang, X. Zou, X. Zhou, W. Zheng, MXene-based quantum dots optimize hydrogen production via spontaneous evolution of Cl- to O-terminated surface groups, Energy Environ. Mater. 0 (2022) 12438–12445, https://doi.org/10.1002/eem2.12438.

[26] S. Sun, X. Zhou, B. Cong, W. Hong, G. Chen, Tailoring the d-band centers endows (Ni$_x$Fe$_{1-x}$)$_2$P nanosheets with efficient oxygen evolution catalysis, ACS Catal. 10 (2020) 9086–9097, https://doi.org/10.1021/acscatal.0c01273.

[27] M. Zhao, W. Li, J. Li, W. Hu, C.M. Li, Strong electronic interaction enhanced electrocatalysis of metal sulfide clusters embedded metal-organic framework ultrathin nanosheets toward highly Efficient overall water splitting, Adv. Sci. 7 (2020) 2001965–2001974, https://doi.org/10.1002/advs.202001965.

[28] B. Wulan, L. Zhao, D. Tan, X. Cao, J. Ma, J. Zhang, Electrochemically driven interfacial transformation for high-performing solar-to-fuel electrocatalytic conversion, Adv. Energy Mater. 12 (2022) 2103960–2103970, https://doi.org/10.1002/aenm.202103960.

[29] W. Yu, Z. Chen, Y. Fu, W. Xiao, B. Dong, Y. Chai, Z. Wu, L. Wang, Superb all-pH hydrogen evolution performances powered by ultralow Pt-decorated hierarchical Ni-Mo porous microcolumns, Adv. Funct. Mater. (2022) 2210855–2210869, https://doi.org/10.1002/adfm.202210855.

[30] Y. Liu, Y. Xing, S. Xu, Y. Lu, S. Sun, D. Jiang, Interfacing Co$_3$Mo with CoMoO$_x$ for synergistically boosting electrocatalytic hydrogen and oxygen evolution reactions, Chem. Eng. J. 431 (2022) 133240–133250, https://doi.org/10.1016/j.cej.2021.133240.

[31] M. Yu, Z. Wang, J. Liu, F. Sun, P. Yang, J. Qiu, A hierarchically porous and hydrophilic 3D nickel–iron/MXene electrode for accelerating oxygen and hydrogen evolution at high current densities, Nano Energy 63 (2019) 103880–103887, https://doi.org/10.1016/j.nanoen.2019.103880.

[32] X. Xu, J. Li, C. Zhang, S. Zhang, G. Su, Z. Shi, H. Wang, M. Huang, Controllable transition engineering from homogeneous NiSe$_2$ nanowrinkles to heterogeneous Ni$_3$Se$_4$/NiSe$_2$ rod-like nanoarrays for promoted urea-rich water oxidation at large current densities, Appl. Catal. B: Environ. 319 (2022) 121949–121958, https://doi.org/10.1016/j.apcatb.2022.121949.

[33] X. Xu, C. Zhang, J. Li, H. Liu, G. Su, Z. Shi, M. Huang, Redistributing interfacial charge density of Ni$_{12}$P$_5$/Ni$_3$P via Fe doping for ultrafast urea oxidation catalysis at large current densities, Chem. Eng. J. 452 (2023) 139362–139370, https://doi.org/10.1016/j.cej.2022.139362.

[34] T. Wang, P. Wang, W. Zang, X. Li, D. Chen, Z. Kou, S. Mu, J. Wang, Nanoframes of Co$_3$O$_4$–Mo$_2$N heterointerfaces enable high-performance bifunctionality toward both electrocatalytic HER and OER, Adv. Funct. Mater. (2021) 2107382–2107390, https://doi.org/10.1002/adfm.202107382.

[35] T. Xiong, B. Huang, J. Wei, X. Yao, R. Xiao, Z. Zhu, F. Yang, Y. Huang, H. Yang, M. S. Balogun, Unveiling the promotion of accelerated water dissociation kinetics on the hydrogen evolution catalysis of NiMoO$_4$ nanorods, J. Energy Chem. 67 (2022) 805–813, https://doi.org/10.1016/j.jechem.2021.11.025.

[36] H. Li, K. Liu, J. Fu, K. Chen, K. Yang, Y. Lin, B. Yang, Q. Wang, H. Pan, Z. Cai, H. Li, M. Cao, J. Hu, Y.-R. Lu, T.-S. Chan, E. Cortés, M. Liu, Paired Ru-O-Mo ensemble for efficient and stable alkaline hydrogen evolution reaction, Nano Energy 82 (2021), https://doi.org/10.1016/j.nanoen.2021.105767.

[37] Y. Ou, W. Tian, L. Liu, Y. Zhang, P. Xiao, Bimetallic Co$_2$Mo$_3$O$_8$ suboxides coupled with conductive cobalt nanowires for efficient and durable hydrogen evolution in alkaline electrolyte, J. Mater. Chem. A 6 (2018) 5217–5228, https://doi.org/10.1039/c7ta11401j.

[38] J. He, Z. Huang, W. Chen, X. Xiao, Z. Yao, Z. Liang, L. Zhan, L. Lv, J. Qi, X. Fan, L. Chen, 0D/1D/2D Co@Co$_2$Mo$_3$O$_8$ nanocomposite constructed by mutual-supported Co$_2$Mo$_3$O$_8$ nanosheet and Co nanoparticle: Synthesis and enhanced hydrolytic dehydrogenation of ammonia borane, Chem. Eng. J. 431 (2022), https://doi.org/10.1016/j.cej.2021.133697.

[39] L. Guo, Q. Chi, J. Zhu, T. Cui, J. Lai, L. Wang, Dual-doping NiMoO$_4$ with multi-channel structure enable urea-assisted energy-saving H$_2$ production at large current density in alkaline seawater, Appl. Catal. B: Environ. 320 (2023) 121977–121986, https://doi.org/10.1016/j.apcatb.2022.121977.

[40] S. Zhou, H. Jang, Q. Qin, L. Hou, M.G. Kim, S. Liu, X. Liu, J. Cho, Boosting hydrogen evolution reaction by phase engineering and phosphorus doping on Ru/ P-TiO$_2$, Angew. Chem. Int. Ed. 61 (2022), e202212196, https://doi.org/10.1002/anie.202212196.

[41] C. Li, Z. Wang, M. Liu, E. Wang, B. Wang, L. Xu, K. Jiang, S. Fan, Y. Sun, J. Li, K. Liu, Ultrafast self-heating synthesis of robust heterogeneous nanocarbides for high current density hydrogen evolution reaction, Nat. Commun. 13 (2022) 3338–3348, https://doi.org/10.1038/s41467-022-31077-x.

[42] K. Wang, S. Wang, K.S. Hui, J. Li, C. Zha, D.A. Dinh, Z. Shao, B. Yan, Z. Tang, K. N. Hui, Dense platinum/nickel oxide heterointerfaces with abundant oxygen vacancies enable ampere-level current density ultrastable hydrogen evolution in alkaline, Adv. Funct. Mater. 33 (2022), https://doi.org/10.1002/adfm.202211273.

[43] Y. Sun, Z. Xue, Q. Liu, Y. Jia, Y. Li, K. Liu, Y. Lin, M. Liu, G. Li, C.Y. Su, Modulating electronic structure of metal-organic frameworks by introducing atomically dispersed Ru for efficient hydrogen evolution, Nat. Commun. 12 (2021) 1369–1377, https://doi.org/10.1038/s41467-021-21595-5.

[44] J. Sun, Z. Zhao, J. Li, Z. Li, X. Meng, Recent advances in transition metal selenides-based electrocatalysts: rational design and applications in water splitting, J. Alloy Compd. 918 (2022), https://doi.org/10.1016/j.jallcom.2022.165719.

[45] C. Qian, W. Shao, X. Zhang, X. Mu, X. Gu, M. Yu, L. Ma, S. Liu, S. Mu, Competitive coordination-pairing between Ru clusters and single-atoms for efficient hydrogen evolution reaction in alkaline seawater, Small 18 (2022) 2204155–2204163, https://doi.org/10.1002/smll.202204155.

[46] S. Shen, Z. Wang, Z. Lin, K. Song, Q. Zhang, F. Meng, L. Gu, W. Zhong, Crystalline-amorphous interfaces coupling of CoSe$_2$/CoP with optimized d-band center and boosted electrocatalytic hydrogen evolution, Adv. Mater. 34 (2022) 2110631–2110638, https://doi.org/10.1002/adma.202110631.

[47] J. Sun, J. Li, Z. Li, C. Li, G. Ren, Z. Zhang, X. Meng, Modulating the electronic structure on cobalt sites by compatible heterojunction fabrication for greatly improved overall water/seawater electrolysis, ACS Sustain. Chem. Eng. 10 (2022) 9980–9990, https://doi.org/10.1021/acssuschemeng.2c02571.

[48] K. Wang, S. Wang, K.S. Hui, H. Gao, D.A. Dinh, C. Yuan, C. Zha, Z. Shao, Z. Tang, K. N. Hui, Synergistically boosting the elementary reactions over multiheterogeneous ordered macroporous Mo$_2$C/NC-Ru for highly efficient alkaline hydrogen evolution, Carbon Energy 4 (2022) 856–866, https://doi.org/10.1002/cey2.188.

[49] J. Sun, X. Meng, Modulating the electronic properties of MoS$_2$ nanosheets for electrochemical hydrogen production: a review, ACS Appl. Nano Mater. 4 (2021) 11413–11427, https://doi.org/10.1021/acsanm.1c02832.

[50] J. Sun, J. Li, Z. Li, X. Hu, M. Bai, X. Meng, Phase transition in cobalt selenide with a greatly improved electrocatalytic activity in hydrogen evolution reactions, ACS Sustain. Chem. Eng. 10 (2022) 4022–4030, https://doi.org/10.1021/acssuschemeng.2c00449.

[51] X.-J. Fang, L.-P. Ren, F. Li, Z.-X. Jiang, Z.-G. Wang, Modulating electronic structure of CoSe2 by Ni doping for efficient electrocatalyst for hydrogen evolution reaction, Rare Met. 41 (2021) 901–910, https://doi.org/10.1007/s12598-021-01819-9.

[52] Y. Tang, Q. Liu, L. Dong, H.B. Wu, X.-Y. Yu, Activating the hydrogen evolution and overall water splitting performance of NiFe LDH by cation doping and plasma reduction, Appl. Catal. B: Environ. 266 (2020), https://doi.org/10.1016/j.apcatb.2020.118627.

[53] T. Wu, M.-Z. Sun, B.-L. Huang, Non-noble metal-based bifunctional electrocatalysts for hydrogen production, Rare Met. 41 (2022) 2169–2183, https://doi.org/10.1007/s12598-021-01914-x.

[54] J. Sun, Z. Huang, T. Huang, X. Wang, X. Wang, P. Yu, C. Zong, F. Dai, D. Sun, Defect-rich porous $CoS_{1.097}/MoS_2$ hybrid microspheres as electrocatalysts for pH-universal hydrogen evolution, ACS Appl. Energy Mater. 2 (2019) 7504–7511, https://doi.org/10.1021/acsaem.9b01486.

[55] F. Zhou, Y. Zhou, G.-G. Liu, C.-T. Wang, J. Wang, Recent advances in nanostructured electrocatalysts for hydrogen evolution reaction, Rare Met. 40 (2021) 3375–3405, https://doi.org/10.1007/s12598-021-01735-y.

[56] H. Roh, H. Jung, H. Choi, J.W. Han, T. Park, S. Kim, K. Yong, Various metal (Fe, Mo, V, Co)-doped Ni_2P nanowire arrays as overall water splitting electrocatalysts and their applications in unassisted solar hydrogen production with STH 14%, Appl. Catal. B: Environ. 297 (2021) 120434–120445, https://doi.org/10.1016/j.apcatb.2021.120434.

[57] Y.S. Park, J. Lee, M.J. Jang, J. Yang, J. Jeong, J. Park, Y. Kim, M.H. Seo, Z. Chen, S. M. Choi, High-performance anion exchange membrane alkaline seawater electrolysis, J. Mater. Chem. A 9 (2021) 9586–9592, https://doi.org/10.1039/d0ta12336f.

[58] J. Sun, Z. Zhang, X. Meng, Low-Pt supported on MOF-derived $Ni(OH)_2$ with highly-efficiently electrocatalytic seawater splitting at high current density, Appl. Catal. B: Environ. 331 (2023) 122703–122712, https://doi.org/10.1016/j.apcatb.2023.122703.